Environment effect on internal fatigue crack propagation studied with in-situ X-ray microtomography

Louis Hebrard [a,*], Jean-Yves Buffiere [a], Thierry Palin-Luc [b,c], Nicolas Ranc [d], Marta Majkut [e], Andrew King [f], Arnaud Weck [g,h,i]

[a] *Université de Lyon, INSA-Lyon, MATEIS, CNRS UMR 5510, Villeurbanne, F-69621, France*
[b] *Univ. Bordeaux, CNRS, Bordeaux INP, I2M, UMR 5295, Talence, F-33400, France*
[c] *Arts et Metiers Institute of Technology, CNRS, Bordeaux INP, Hesam Universite, I2M, UMR 5295, Talence, F-33400, France*
[d] *PIMM Laboratory, Arts et Metiers Institute of Technology, CNRS, Cnam, HESAM University, 151 Boulevard de l'Hôpital, Paris, F-75013, France*
[e] *ESRF—The European Synchrotron, 71 avenue des Martyrs, BP 220, Grenoble Cedex 9, F-38043, France*
[f] *Synchrotron SOLEIL, L'Orme des Merisiers Saint-Aubin, Gif-sur-Yvette, F-91192, France*
[g] *Department of Mechanical Engineering, University of Ottawa, 150 Louis Pasteur, Ottawa, ON, K1N 6N5, Canada*
[h] *Centre for Research in Photonics, University of Ottawa, 25 Templeton, Ottawa, ON, K1N 6N5, Canada*
[i] *Department of Physics, University of Ottawa, 150 Louis Pasteur, Ottawa, ON, K1N 6N5, Canada*

ABSTRACT

Keywords:
Fatigue
Internal crack
Environment
Synchrotron
Ultrasonic
Short crack

In the present study, physically short fatigue cracks initiated from an artificial internal notch under vacuum conditions are observed in smooth specimens made of titanium alloy. The crack initiated from such a notch is not in contact with the surface during the majority of its propagation. Another batch of artificially notched specimens in the same alloy having their internal notch linked with the surface to bring air to the initiated short crack were tested too. All the specimens were ultrasonically cycled with synchrotron micro-computed tomography acquisitions which were regularly acquired from crack initiation detection to final failure without demounting the specimen. The number of cycles to failure, the internal crack growth rate and the crack growth mechanisms of internal cracks are compared for propagation under either air conditions or in the core of the alloy (*i.e.* under vacuum environment). It is shown that the environment plays a key role in the explanation of the very low crack growth rate of internal short crack loaded at very low stress amplitude leading to the gigacycle regime.

1. Introduction

The majority of high cycle fatigue cracks initiate from the specimen surface. However, for very low stress amplitudes, the probability to observe initiation sites in the interior of the material increases [1–4]. Such internal fatigue crack initiations could lead to important industrial problems as explained by [5–7] but experimental methods to study this type of crack are very limited. Indeed, most of the experimental references on internal fatigue cracks are focused on the total number of cycles and post-mortem observations of the final fractured surfaces as reviewed by [8].

There are three ways to follow internal crack propagation with an in-situ approach, *i.e.* by observing the crack during its propagation in a non-destructive way and not after the final failure. Literature contains examples of internal crack growth monitored with real-time infrared camera [9–11]. In the case of ultrasonic loading, the real-time analysis of the displacement non-linearity parameter is also a tool to detect an internal crack propagation [12]. However, the most promising method is the use of X-ray micro-computed tomography (μCT) to directly access the crack shape in 3D at several instants of its propagation. This imaging method has been used to study fatigue crack propagation as shown in recent reviews [13,14]. The influence of environment on 3D crack propagation has been observed for example in presence of humidity [15] or in vacuum by imaging internal crack propagation. [16–18] could detect many internal cracks in a single Ti alloy specimen with a synchrotron μCT approach. [19] have followed a crack that initiated from an internal casting defect in an Al alloy and [20] could detect an internal crack initiation from an inclusion in a Ni-based super-alloy also with this method. The present work is based on the experimental protocols presented by [21–23] who could observe internal crack propagation in a casting Al alloy and a Ti64 alloy using an in-situ synchrotron μCT technique.

With access to the 3D shape of the propagating internal cracks, it is possible to quantify the crack growth rate. Indeed, without this tool, the evolution of an internal crack was deduced from typical features on the final fracture surface such as striations when they are present on the fractography [24,25]. This crack growth rate parameter can be used to compare the propagation of surface and internal cracks and to examine the differences between both cases. Particularly, the environment may have a crucial role on crack propagation as pointed out by numerous publications. The model from [26] states that hydrogen-caused embrittlement leads to higher crack growth rates under air environment. Corresponding experimental evidences have been made on Ti64 by [27–29] but also on other Ti alloys by [30,31] or [16] (see also [32] and [33] for reviews). In all these studies, the fatigue crack growth rate is lower under vacuum conditions than it is in air environment. However these observations have been carried out in the high cycle fatigue regime. To study the impact of the environment on crack propagation, the vast majority of studies use surface long cracks [29,30] or CT specimens [34] which are placed in a vacuum chamber before to compare the results with data obtained with the same protocol under air environment.

To evaluate the influence of the environment, this study combines the artificial internal notch procedure described in [23] and the ultrasonic in-situ synchrotron setup developed by [21]. The artificial internal notches are known to be under vacuum conditions [22] unless a path is added to link the initiation site to the surface in order to bring air to the propagating crack [35]. With this experimental method, crack shapes and crack tip stresses for samples with an internal crack exposed to air environment and samples with an internal crack under vacuum can be directly compared. Ultrasonic cycling allows to study physically short cracks propagating in the Very High Cycle Fatigue (VHCF) domain and synchrotron-µCT acquisitions provide 3D-data used to compare internal crack growth rates in air and vacuum conditions.

2. In-situ synchrotron setup

2.1. Ultrasonic fatigue testing machine

An ultrasonic fatigue machine adapted to in-situ micro-computed tomography provided by synchrotron facilities has been previously developed [21]. This apparatus has been adapted to the ultrasonic cycling of Ti64 samples which is carried out at higher stress amplitudes than the cast aluminum samples studied in the previous paper. This apparatus is composed of a piezoelectric converter which is powered by a 20 ± 0.5 kHz ultrasonic generator and cooled down by dry compressed air. Between this converter and the specimen, a booster and a horn amplify the ultrasonic vibration in order to cycle the specimen in tension–compression with a loading ratio of $R = -1$.

A laser vibrometer monitors the free-end surface displacement of the specimen during the cycling in order to detect a non-linearity that may be caused by a crack initiation. The output signal of the laser conditioner is treated in real-time and used to automatically stop the ultrasonic vibration when the non-linearity reaches a threshold (this aspect of the protocol is described in detail in Section 2.2).

The vibration nodes of the booster are clamped with the structural tube and a force sensor located on the two clamping parts of the machine allows to measure the applied static load on the specimen during µCT acquisitions. The value of such a load is fixed at 80% of the stress amplitude to open the initiated crack in the loading direction (mode I) in order to better distinguish it on the µCT data [17].

2.2. Experimental protocol

The experimental procedure is divided in two phases: the crack initiation and the crack growth monitoring.

The *initiation phase* consists in the cycling of the specimen with the machine described in Section 2.1. It is carried out at room temperature and the specimen is not cooled down during the cycling but its surface temperature is monitored with an infrared camera and remains under 40 °C. This thermal data will be presented and analyzed in a future study (it can be used to monitor the crack growth rate as already done by [11]). The laser vibrometer monitores the bottom-surface displacement of the specimen (the machine is in its cycling mode depicted by Fig. 1a), there is no tensile static force applied on the specimen during its vibration at 20 kHz. With a real-time fast Fourier transform (FFT) of the vibration of the specimen free-end, it is possible to obtain in real time the values of the fundamental, U_1, and the second harmonic, U_2, of this signal. Based on the work of [12], a non-linear parameter, α, can be computed (Eq. (1) where $(.)_0$ represents the value of $(.)$ at the beginning of the cycling).

$$\alpha = 20 \log_{10}\left(\frac{U_2}{U_1^2}\right) - 20 \log_{10}\left(\frac{U_2}{U_1^2}\right)_0 . \qquad (1)$$

This α parameter characterizes the non-linearities of the whole system: non-linearity of the material in the elementary representative volume, non-linearity due to the potential onset of a macroscopic crack and non-linearity coming from the horn, the booster and the converter. The notation α – which differs from the one used in [12] – is used to avoid any confusion with the non-linear parameter β used in the non-linear acoustic community for the quadratic term of the non-linear Hooke's law. The experiment environment may have an impact on this non-linearity. Consequently, in order to ensure good reproducibility of the ultrasonic fatigue test and detection by this technique, the compressed air used to flow the converter has to be stable and the temperature of the testing room is stabilized during the test (air conditioning). Using this approach, the ultrasonic cycling can be stopped when the α parameter reaches a threshold value. Once a potential crack initiation has been detected, the cycling is automatically stopped and a static load is applied to the specimen (80% of the stress amplitude that is also 80% of the maximum stress because our tests were carried out under $R = -1$). A µCT acquisition is then carried out (machine in its acquisition mode in Fig. 1b).

On the PSICHE beamline (SOLEIL synchrotron), we use a multi-bunch 65 keV pink beam which has been filtered with a 3 mm Al + 0.304 W plate. With a 4608 × 2592 pixels Hamamatsu ORCA Lightning camera, a $1.5 \times 3.2 \times 3.2$ mm³ volume with a voxel size of 0.723 µm can be acquired with a 360 degrees acquisition containing 7000 projections (for better statistics and fewer artifacts). The scan duration takes approximately 10 min. On ID19 beamline (ESRF), a multi-bunch 70 keV pink beam is available. With a 2160 × 2560 pixels detector and a half-acquisition setup (5300 projections and exposure time of 0.1s), the $1.5 \times 3.2 \times 3.2$ mm³ volume can be acquired in 10 min with a voxel size of 0.7 µm. The reconstruction time takes typically 15 min so, in less than half an hour, the 3D data from the µCT acquisition is available. When an automatic testing stop happens, it is always necessary to carefully verify that it is due to a crack initiation. Indeed, some false detections can occur due to the detection technique being very sensitive to parasitic vibrations. If no crack is detected on the 3D data, the initiation phase continues as described above, but if an initiated crack is observable from the µCT data, the procedure shifts to the propagation phase.

During *the propagation phase*, the number of cycles is pre-set so that the ultrasonic cycling is not controlled by the laser vibrometer anymore. Even if this detection system is still active, to prevent the initiated crack to propagates too quickly, each loading block is limited in number of cycles (typically between 10^4 and 5×10^6 cycles that is 0.5 to 250 s) to more precisely control the crack propagation between two successive µCT acquisitions. µCT data obtained with such a testing method are presented in Section 4.
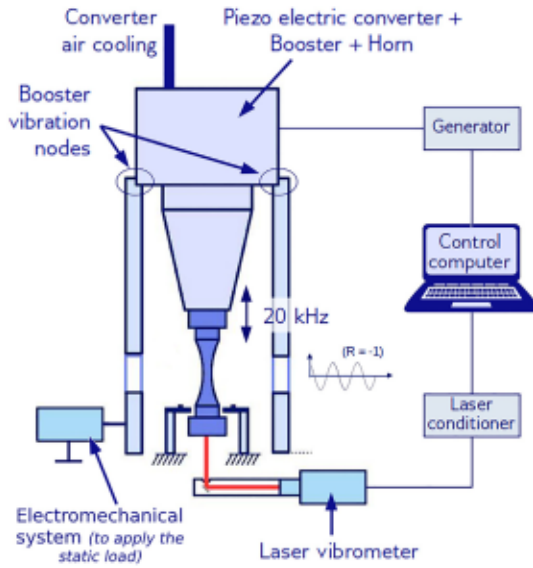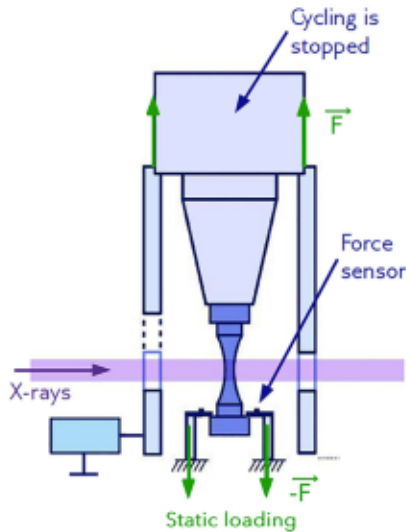
Fig. 1a. Cycling mode of the machine.

Fig. 1b. µCT acquisition mode of the machine.

3. Material and specimens

The material used here is a Ti64 alloy which is frequently used in aeronautics particularly for turbine blades which can undergo cyclic loadings up to more than 10^7 cycles [36]. The chemical composition of this alloy provided by Timet is given in Table 1. This hot-rolled titanium alloy has been annealed at 750 °C. As represented in Fig. 2a, its equiaxed microstructure is composed of small bcc β zones located at the boundaries between bigger hcp α regions (surface fraction $\sim$ 94%). The average α grain size determined from area fraction measurement in Electron Backscatter Diffraction (EBSD) maps (Fig. 2b) is 10 $\pm$ 1 µm. A 5° grain tolerance angle (minimum misorientation between adjacent grains) has been used for this approach.

As described in Section 2, the specimens were designed in order to have their first longitudinal eigen mode at 20 $\pm$ 0.5 kHz. For that purpose, an axisymmetric specimen geometry is first approximated by a 1D-model which neglects the Poisson effect [6]. This model provides a first design of the specimens. The geometry is then imported in the finite element analysis software Abaqus to obtain a design which

Table 1
Chemical composition of the studied Ti64 (mass%).

Al	V	Fe	O	C	N	H	Y	Ti
6.43	4.10	0.15	0.18	0.01	0.004	0.004	<0.001	Bal.

integrates special heads to apply a static loading during tomography (cf. Fig. 3c) and a first longitudinal eigen mode at 20 kHz. This step is also an opportunity to verify if the other eigen modes are not in the 20 $\pm$ 2 kHz range to avoid any parasitic mode.

In order to ensure internal crack initiation but also to know its precise location (to facilitate the µCT observation), an artificial internal notch is inserted inside the specimen by following the procedure described by [22,23]. It is also possible to add a narrow path – which is called *chimney* in the rest of this paper – to link the notch to the surface of the specimen to bring air to the internal notch. Discussion on the level of vacuum in the artificial notch with and without the optional laser-drilled chimney can be found in [23]. The notching procedure is illustrated in Fig. 3 and the list of tested specimens is available in Table 2. All stress amplitude values given in this paper are the nominal values *i.e.* the average stress amplitudes dynamically calculated over the middle cross section of the specimen without considering the presence of the notch or the crack. The chimney presence is neglected too for the stress calculation.

The fabrication steps are as follows:

- With electrical discharge machining technology, a 15-mm-thick Ti64 sheet is cut in its middle in two parts which are mechanically polished down to 1 µ m (with silica suspension).
- One half-sheet is notched with the use of a femtosecond laser (which produces short and reduced interaction with the material) as described in [23]. This The notch dimensions are approximately 300 × 120 × 20 µm (cf. Fig. 3a). For the second type of specimen whose notch is in contact with ambient air during fatigue cycling, a chimney (with a 170 × 50 µm section) links the central notch to the bottom surface of the specimen (cf. green volume in Fig. 4c). It is important to specify that the notching protocol is easily reproducible and every specimen presented in this study has been notched from the same batch. Hence, every notch is geometrically quasi-similar to the others (cf. Fig. 4). As depicted by Fig. 4a, the µCT voxel size is not small enough to determine if the opening created by the laser in the central part of the notch is very thin or if it has been rewelded during the thermal treatment. However, such internal notches allow the cracks to initiate which is their primary objective as this study focuses on crack propagation.
- The two halves are diffusion bonded using Spark Plasma Sintering (SPS) technology (cf. Fig. 3b). The thermal bonding protocol has been previously developed [22] and starts by applying a 1 MPa initial loading between the two half-sheets while a primary vacuum is pumped down to 100 Pa. A compressing 15 MPa force is then applied before to increase the temperature up to 750 °C with a heating rate of 100 °C/min. These 750 °C are maintained during 10 min before to control the temperature decrease down to 450 °C with a decrease rate of 25 °C/min (in order not to have microstructural change due to a strong cooling). The last step is natural cooling in the SPS chamber down to 200 °C. The diffusion bonding temperature is the same than the one applied during the one hour hot-rolling (used to form the initial titanium plates). The short duration of this SPS protocol explains the similar aspect of microstructure before and after the bonding.
- After SPS, the internal notch position is checked with X-ray radiography before specimen manufacturing.
- Finally, when the specimen has been manufactured (Fig. 3c), the gauge lengths are manually polished (down to 4000 grit SiC paper) in order to avoid surface crack initiation due to the lathe machining marks on the specimen.
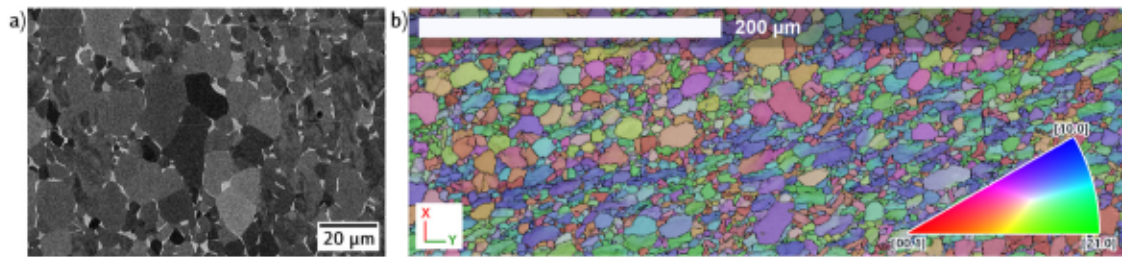
Fig. 2. Ti64 microstructure observed with (a) SEM back-scattered (b) EBSD (map along the rolling direction Z).
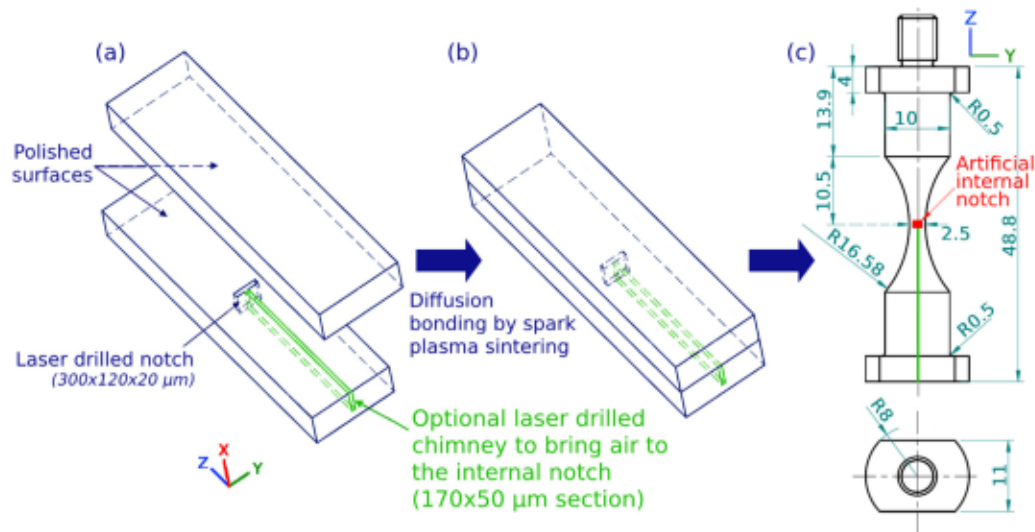

Fig. 3. Specimen fabrication process: (a) one half-sheet with an artificial notch is sintered with another unnotched half-sheet. (b) sintered sheet used to manufacture the specimen. (c) final specimen geometry (dimensions in mm). The green chimney is optional and can be added to bring air to the internal notch. (For interpretation of the references to color in this figure legend, the reader is referred to the web version of this article.)

Table 2
List of the specimens tested in this study.

Specimen n°	Notch type	Crack environment	Stress ampl. (MPa)	Nb of cycles before failure	Nb of cycles at 1st µCT acq.	Corresponding marker in Fig. 9a
43	Notch only	Vacuum	385	1.05×10^8	No µCT data	/
44	Notch only	Vacuum	337	1.17×10^8	9.59×10^6	⬤
45	Notch only	Vacuum	329	7.53×10^7	9.73×10^6	⬤
46	Notch only	Vacuum	330	4.55×10^7	9.98×10^6	⬤
55	Notch only	Vacuum	330	1.30×10^8	No µ CT data	/
61	Notch only	Vacuum	330	8.92×10^7	7.18×10^7	⬤
58	Notch only	Vacuum	500	2.43×10^6	2.06×10^6	⬤
59	Notch only	Vacuum	500	3.38×10^6	No µCT data	/
48	Notch + chimney	Air	300	5.04×10^5	3.70×10^5	🟧
49	Notch + chimney	Air	315	8.16×10^5	No µ CT data	🟩
52	Notch + chimney	Air	300	4.02×10^5	3.49×10^5	🟥
53	Notch + chimney	Air	300	3.60×10^5	6.21×10^4	⬜

4. Experimental results and discussion

4.1. Wöhler curves

The experimental fatigue data are shown in a Wöhler diagram in Fig. 5a and 5b. Some specimens without any artificial notch but with the same geometry (Fig. 3c) were cycled to failure (violet points in Fig. 5a). The Wöhler data for these specimens without artificial notches are comparable with other studies on the same alloy ($R = -1$) [2, 4,34,37–41]. Unless specified in the legend, all points from the cited studies correspond to Ti64 alloy specimens cycled in air environment with a loading frequency of 20 kHz and a loading ratio of $R = -1$. For stress amplitudes ranging between 500 and 650 MPa, the fatigue lives of this Ti64 alloy are scattered and the samples with the longest lives tend to fail from internally initiated cracks.
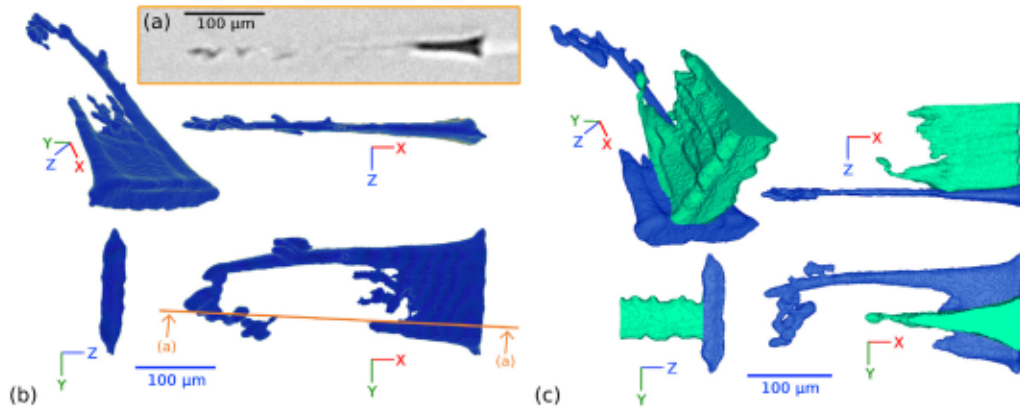
Fig. 4. (a) Section of a notch without the chimney. 3D views of an internal notch (b) without and (c) with the chimney which can bring air to the internal crack. The chimney is displayed in green. (The loading direction is along *z*.). (For interpretation of the references to color in this figure legend, the reader is referred to the web version of this article.)
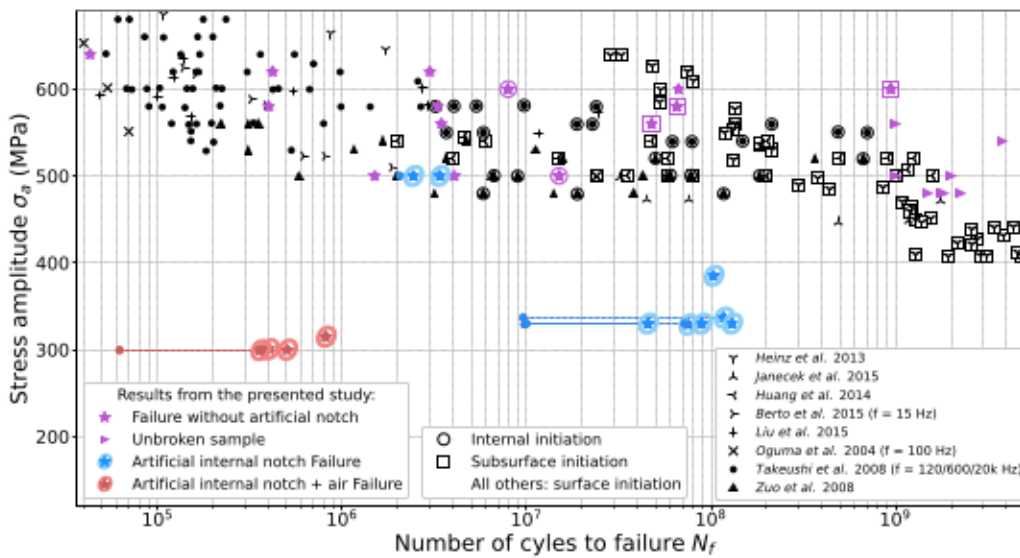

Fig. 5a. Wöhler diagram comparing results from this work and from literature. The horizontal dashed lines represent the number of cycles between the crack first detection and final failure (values in Table 2).
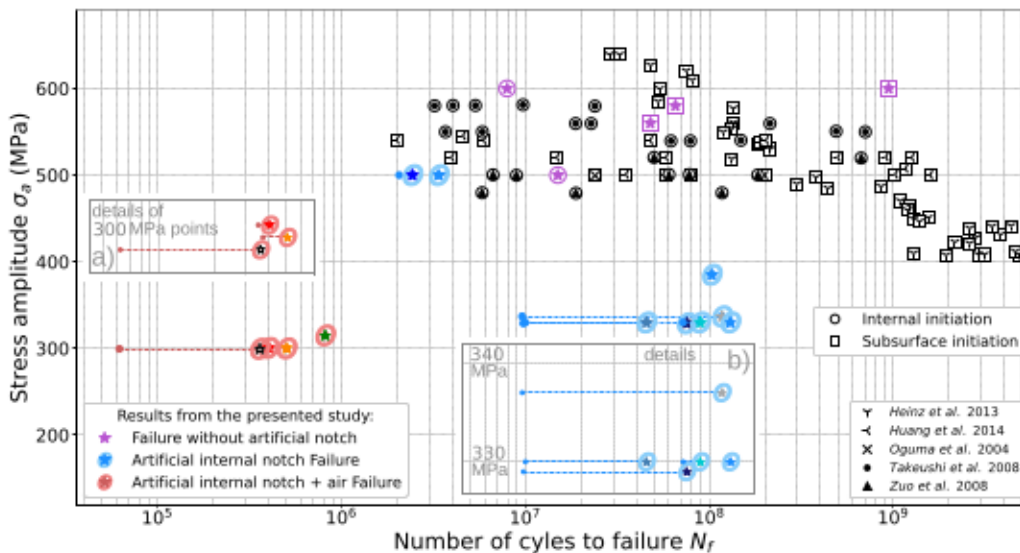

Fig. 5b. Wöhler diagram comparing results from this work and from literature *for internal or subsurface initiation only* (no surface crack initiation). The specimens color code is given in Table 2. All points in inset (a) have a 300 MPa stress amplitude whereas inset (b) presents points with different stress amplitudes.

Data obtained from our specimens broken by propagation from an *internal crack not in contact with air* are represented in Fig. 5b. The horizontal dashed lines shown in inserts represent the number of cycles between the first crack detection (initiation) and final failure; these data can only be acquired with the use of in-situ µCT. The figure shows that the insertion of the artificial internal notch shortens the fatigue lives and reduces their scatter. The first in-situ crack initiation detections are also similar between the artificially notched specimens cycled at the same stress amplitude.

Finally, this Fig. 5b comprises also data from specimens with an *artificial internal notch cycled in air environment*. The number of cycles before failure is two orders of magnitude lower than for similar cracks under vacuum conditions. Interestingly, very good reproducibility can also be observed in this case.

4.2. µCT data

The experimental protocol described in Section 2.2 was performed at room temperature on several specimens and provided tomographic data as shown in Fig. 6 for a specimen with an internal notch in contact with air.
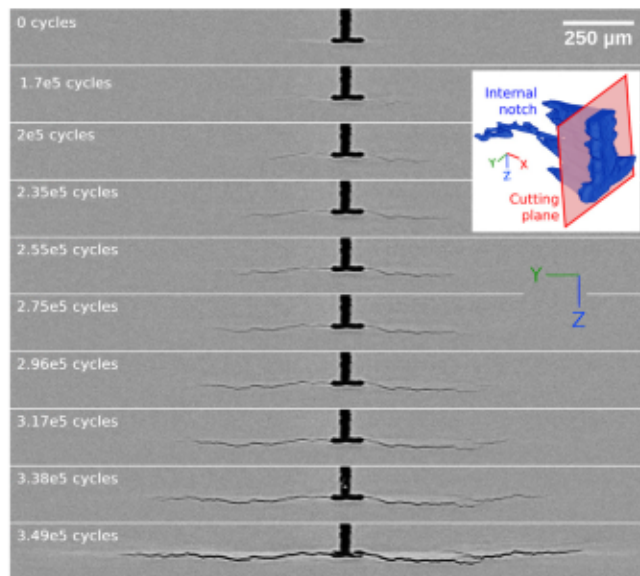

Fig. 6. Reconstructed tomographic slices showing the propagation of an internal crack in contact with air — stress amplitude of 300 MPa and loading direction parallel to Z (specimen n° 53). The chimney which brings the air from the top to the internal notch is visible on the slices.
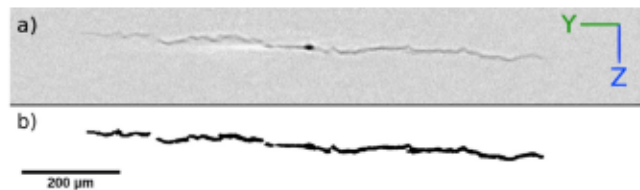

Fig. 7. (a) Initial grey level of a reconstructed slice of an internal crack after 4.4×10^7 cycles of propagation under vacuum with a stress amplitude of 330 MPa (specimen n° 46). (b) Binary image after the thresholding protocol (cf. Appendix B) for the same slice. The location of this section in the 3D volume is represented in Fig. 8.

The µCT data is used to obtain a 3D volume of the crack at different instants of its propagation. An automatized thresholding protocol has been developed with the use of `ImageJ` software to convert each 8-bit µCT stack dataset into a binary stack representing the propagated crack. It is described in detail in Appendix B. The initial and final step of the procedure is illustrated for a 2D slice in Fig. 7. The thresholding protocol provides the 3D shape of the cracks at different propagation stages.

These data can be used to visualize the crack shape and to measure their size (cf. Section 4.3). Fig. 8 represents the projections on a plane perpendicular to the loading axis of the binarized crack at different numbers of cycles for a propagation under vacuum environment.

4.3. Crack growth kinetics and Paris diagram

The crack fronts after different numbers of cycles are used to plot the crack growth rate curves ($da/dN = f(\Delta K)$ with a the crack size, N the number of cycles and ΔK the Stress Intensity Factor range). To the best of the authors' knowledge, such experimental data could not be found in the literature for a **titanium alloy ultrasonically cycled with a stress ratio R = -1** (either under air or under vacuum environment propagation condition).

For this paper, an equivalent crack size a_{eq} is evaluated from the 3D projected crack area as it was done in the method described in [22]. a_{eq} corresponds to the radius of a disk (*i.e.* penny shape crack) with the same area as the projected crack: $a_{eq} = \sqrt{area/\pi}$. This value is a very good average of the various crack sizes along the crack front [22].

The thresholding protocol described in Section 4.2 could not be carried out for specimens n° 44 and 45 because of the presence of numerous artifacts in the 3D images. For these two specimens, the crack equivalent radius was approximated by half the maximum crack dimension measured from 2D sections of the µCT acquired volume.
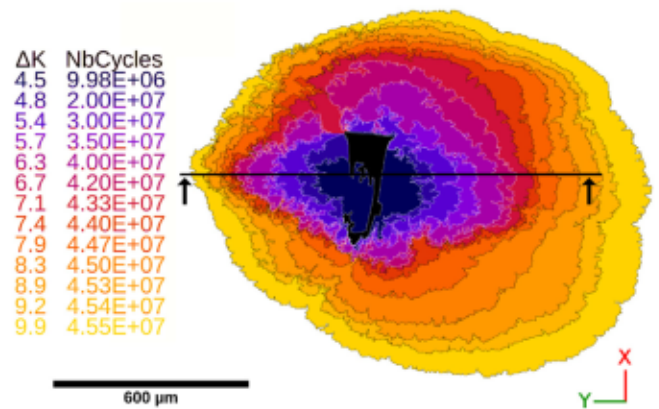

Fig. 8. Crack shape projections at different propagation stages on a plane perpendicular to the loading direction. The stress amplitude is 330 MPa with a vacuum environment (specimen n° 46). The cutting plane indicated by arrows corresponds to the section depicted in Fig. 7. The displayed Stress Intensity Factor range ΔK is calculated as detailed in Section, 4.3.

The value of the Stress Intensity Factor (SIF) range ΔK is estimated from the formulation of [42] (Eq. (2)). This equation is valid for a penny-shape crack at the center of a specimen with a circular cross-section. This penny-shape has been assumed all along the fatigue life including the early stages of propagation where some cracks can have irregular 3D fronts (cf. the darker shapes of Fig. 8). Such hypothesis entails an uncertainty on the measurement, it has been quantified and is detailed in Appendix A. This simple analysis does not take into account the crack eccentricity. Additional numerical simulations could take into account more accurately the 3D crack geometry and its location in the section (this will be done in a future study). The proposed simplified data analysis used here mainly aims at *comparing* an internal crack propagating in air or in vacuum and *comparing* this with data from the literature.

$$\Delta K = \frac{2}{\pi} \Delta\sigma \sqrt{\pi a_{eq}} \; \frac{1 - \frac{a_{eq}}{2b} + 0.148 \left(\frac{a_{eq}}{b}\right)^3}{\sqrt{1 - a_{eq}/b}}, \tag{2}$$

with $\Delta\sigma = \sigma_{max} - \sigma_{min}$ the stress range, a_{eq} the equivalent crack size (radius) and b the radius of the specimen gauge length.
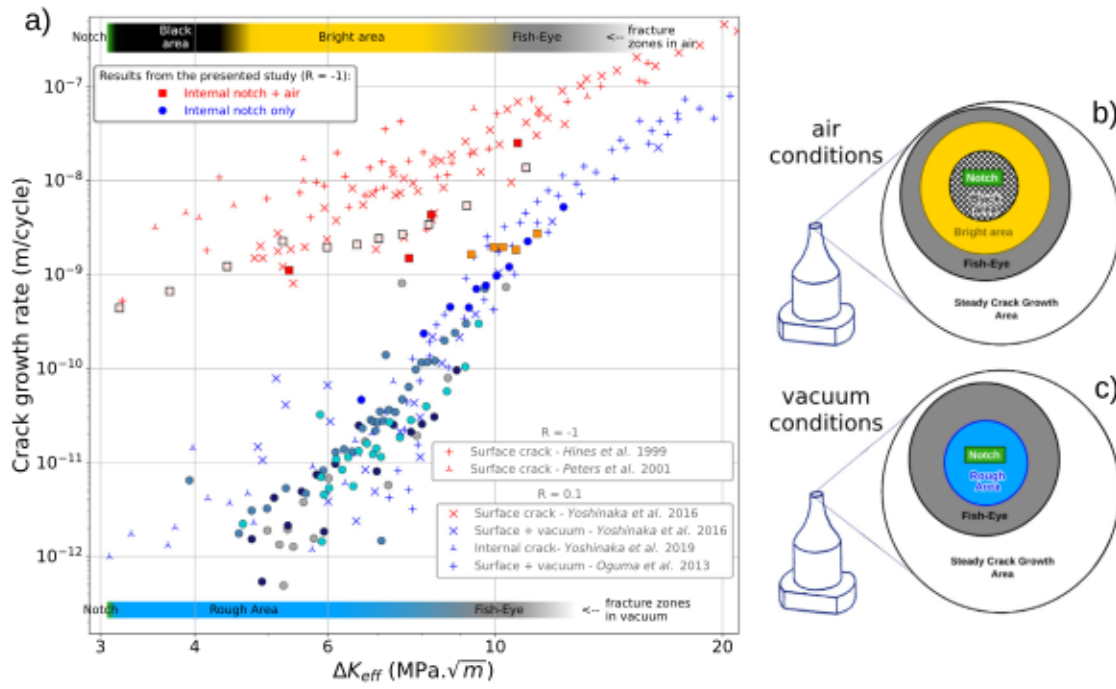
Fig. 9. (a) Crack growth rate data of the tested specimens in a Paris diagram. Data from the cited studies were all run at "low" loading frequency (between 30 and 400 Hz). Table 2 links each marker type with a specimen. The SIF range corresponding to the different regions of the fracture surfaces in vacuum and in air are shown by the colored bars respectively at the bottom and at the top of the curve as explained in Section 4.4. Scheme of the fracture surface for a crack which propagated in air (b) and vacuum (c) environment. (For interpretation of the references to color in this figure legend, the reader is referred to the web version of this article.)

It is generally supposed that the crack does not propagate when it is closed. Consequently the effective SIF range ΔK_{eff} is approximated as $\Delta K_{eff} = K_{max} - K_{op}$ with K_{op} the minimum SIF value for which the crack is open. With an ultrasonic loading at 20 kHz, according to the authors' knowledge, it is not possible to experimentally determine the value of K_{op}. Hence, as the cycling was carried out under a loading ratio of $R = -1$, the crack is supposed to be closed when the applied stress is negative ($K_{op} = 0$ and $\sigma_{max} = \Delta\sigma/2$). Eq. (2) then transforms as follows:

$$\Delta K_{eff} \approx \frac{2}{\pi} \frac{\Delta\sigma}{2} \sqrt{\pi a_{eq}} \; \frac{1 - \frac{a_{eq}}{2b} + 0.148 \left(\frac{a_{eq}}{b}\right)^3}{\sqrt{1 - a_{eq}/b}}, \qquad (3)$$

with $\Delta\sigma/2 = \sigma_a$ the stress amplitude.

The crack growth rate $\frac{da}{dN}$ is estimated from the crack size difference between two successive scans. It is linked with an average of the two SIF evaluated for these two scans in order to obtain Fig. 9a. The estimated value is in fact the mean value of the crack growth rate. The corresponding uncertainties on these measurements are detailed in Appendix A.

Fig. 9a compares the crack growth rate data from this study with experimental data from literature [28,29,43–45]. The circle symbols correspond to specimens cycled with an internal crack under vacuum conditions and the square symbols correspond to specimens with an internal crack in contact with air (see Table 2). Reference data comprise some cracks which initiated from the surface in an air environment (red markers) and some cracks which had either internal initiation or surface initiation under vacuum condition (blue markers). No literature data could be found for cracks under vacuum conditions at $R = -1$. Therefore, our vacuum-propagated crack data could only be compared with literature experiments carried out at $R = 0.1$. Fig. 9a shows that, in agreement with the literature, for the same SIF range, the crack growth rates are higher for cracks in contact with air – even when these are internal cracks – compared to internal cracks propagating under vacuum conditions. To the best of the authors' knowledge, this is the

first time that *direct* measurements of growth of *internal fatigue cracks in air* are reported. These experimental data point out the key role of environment on the kinetics of internal physically short cracks. This aspect will be discussed in Section 4.5.

4.4. Fracture surface analysis

The two crack surfaces of the broken fatigue specimens were analyzed with optical microscopy and Scanning Electron Microscopy (SEM). Representative examples of the pictures obtained during this fractographic analysis are shown in Fig. 10 for internal crack propagation under vacuum environment and in Fig. 11 for internal crack propagation under air conditions.

For **internal cracks without contact with air** (*i.e.* under **vacuum conditions**), the crack surfaces include the standard features observed for internal initiation in a Ti64 alloy. As described by [8], the crack surface comprises three zones which can be distinguished for all the specimens cycled under vacuum environment (cf. Fig. 9c):

- A dark area is present in the vicinity of the initiation site. In this so-called *Rough Area*, the crack has a strong interaction with the microstructure which results in a relatively large roughness. More precisely, the zone is composed of smooth facets dispersed within granular areas (cf. Fig. 10b). This is in agreement with the observations of [28,40,46] for the same type of alloy.
- A circular zone surrounds the Rough Area, this more planar area is called the *Fish-eye* zone. Even if this zone is less contrasted than the Rough Area, it can be distinguished in Fig. 10a.
- Finally, the *Steady Crack Growth Area* composes the last part of the fracture surface where the SIF reaches the material toughness and propagates quickly.
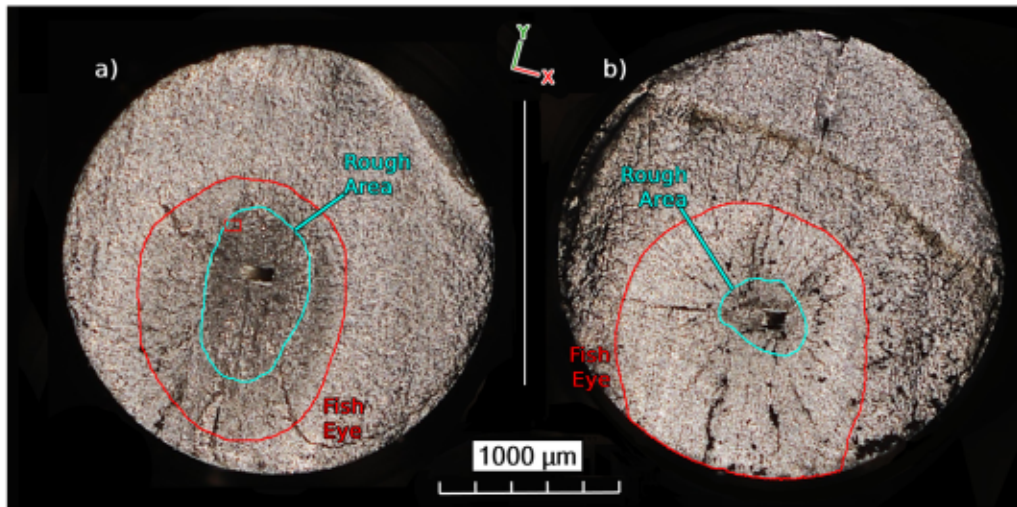
Fig. 10a. Optical view of one side of two different fracture surfaces with internal crack propagation without contact with air *i.e.* under vacuum environment. (a) (specimen n° 46). (b) (specimen n° 59). The Rough-Area surrounds the initiation site and is comprised into a circular Fish-Eye zone. The red rectangle locates Fig. 10b; based on Eq. (3), an average value of $\Delta K \approx 6.7$ MPa $\sqrt{\text{m}}$ is determined in this region. (For interpretation of the references to color in this figure legend, the reader is referred to the web version of this article.)
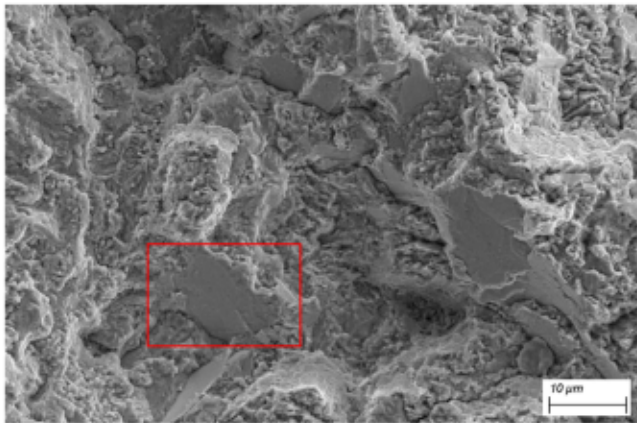

Fig. 10b. SEM zoom on the rough area with facets separated by granular zones. The red rectangle locates Fig. 10c. (For interpretation of the references to color in this figure legend, the reader is referred to the web version of this article.)
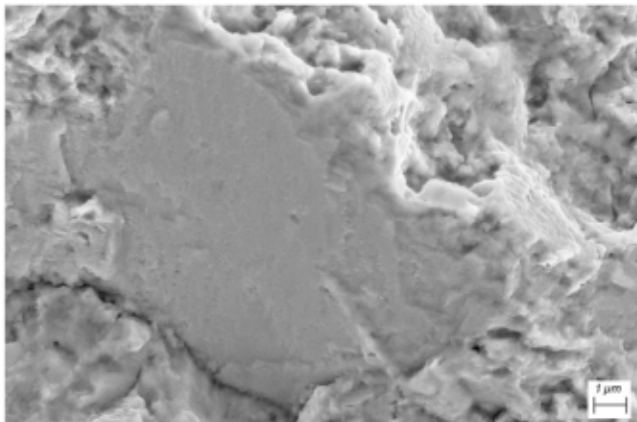

Fig. 10c. SEM zoom on a facet located in the rough area.

For **internal cracks propagating in air environment** a different crack surface aspect has been observed. Fig. 11a depicts two different zones around the initiation site and inside the Fish-Eye region (cf. Fig. 9b):

- The smaller zone which is located in close vicinity of the initiation location appears very dark on optical microscope observations and therefore will be called the *black area*. Its faceted aspect seems to be characteristic of strong interactions of the crack with the microstructure (Fig. 11b).
- On the contrary, the zone which surrounds this dark central region appears bright on optical observation and is more planar than the rest of the crack surface (Fig. 11d). The facets located in this zone very frequently present extensive striations (cf. Figs. 11e and 11f).

According to the literature, the presence of striations is specific to crack propagation under air environment. Two possible mechanisms have been proposed: [47] postulated that, in a vacuum environment, the absence of any oxide layer will enhance the rubbing marks on the crack surfaces and will obliterate the fatigue striations; a different hypothesis from [48] claims that, in air, the oxide layer prevents the shear process to be reversible and leads to the formation of a striation pattern. In our study, striations could be observed only on the fatigue crack surfaces which are in contact with air and not on the facets of cracks which propagated in vacuum (cf. Fig. 10c). The inter-striation spacing has been used to locally estimate the crack growth rate within the facets. For this, the crack is assumed to propagate of the distance measured between two striations in one cycle. The measurements have been carried out for at least 10 facets per specimen at ΔK values ranging from 4 to 10 MPa $\sqrt{\text{m}}$. The resulting crack growth rate does not seem to vary with ΔK values, its average value is $2.7 \times 10^{-7} \pm 1.0 \times 10^{-7}$ m/cycle. This local crack growth rate is two orders of magnitude higher than the maximum value of the macroscopic one which has been determined from µCT data. This observation matches with the results from [49] who measures a value of 1.4×10^{-7} m striation spacing when $\Delta K = 18$ MPa $\sqrt{\text{m}}$ for a crack under air environment in the same alloy cycled at $R = 0.1$. A possible explanation for this apparently high crack growth rate in the facets is that the crack in the flat facets could stay arrested during several cycles (between 10 and 100) before propagating again. Another explanation lies in the fact that the propagation is not homogeneous along the crack front so the macroscopic crack growth
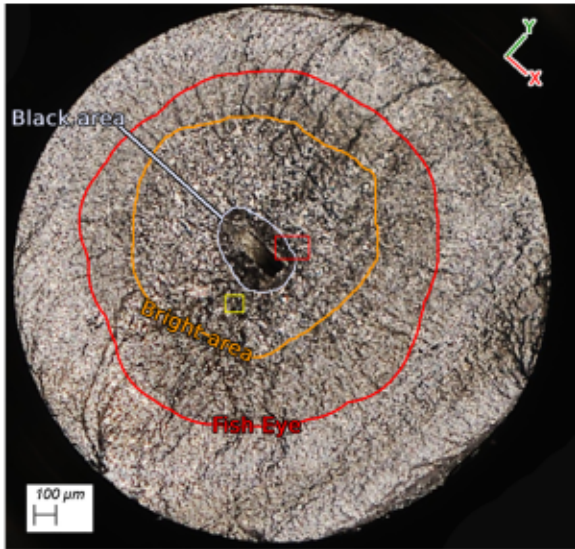
Fig. 11a. Optical view of the fracture surface containing an internal crack which propagated under air environment (specimen n° 48). A black area surrounds the initiation site and is comprised within a bright area which is itself in the Fish-Eye zone. The red rectangle locates Fig. 11b. Figs. 11d–11f are located in the yellow rectangle where the value of the SIF range is estimated at $\Delta K \approx 5.4$ MPa $\sqrt{m}$ (Eq. (3)). (For interpretation of the references to color in this figure legend, the reader is referred to the web version of this article.)
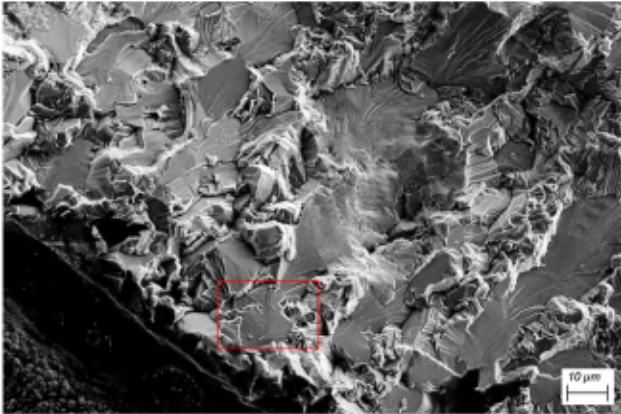

Fig. 11b. SEM zoom on the black area with crystallographic aspect located in the red rectangle of Fig. 11a. The red rectangle locates Fig. 11c. (For interpretation of the references to color in this figure legend, the reader is referred to the web version of this article.)
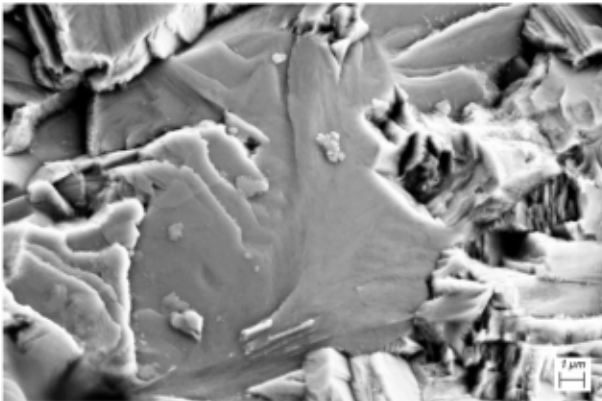

Fig. 11c. SEM zoom on a facet from the dark zone located in the red rectangle of Fig. 11b.
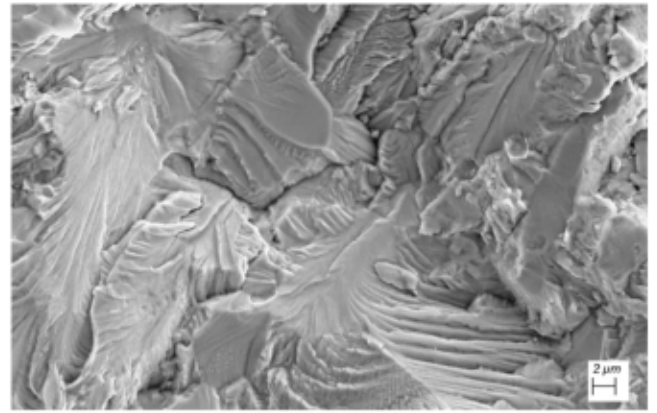

Fig. 11d. SEM zoom on the bright zone with planar aspect located in the yellow rectangle of Fig. 11a.
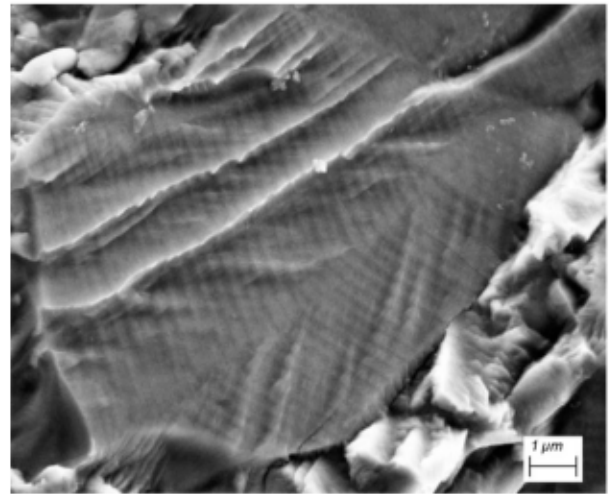

Fig. 11e. SEM zoom on a facet from the bright zone showing extensive striations located in the yellow rectangle of Fig. 11a.
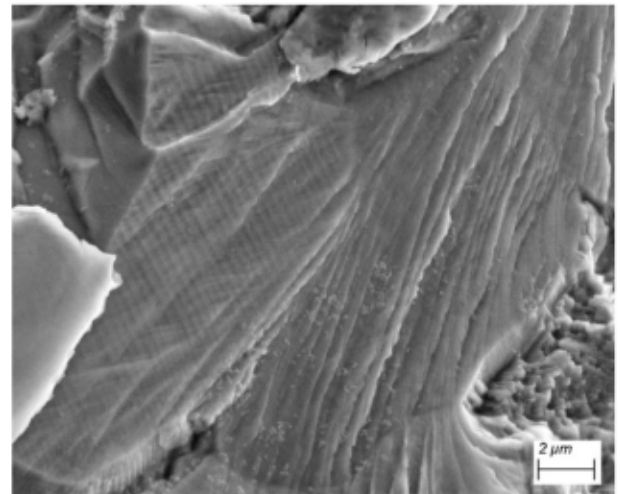

Fig. 11f. SEM zoom on a facet from the bright zone showing extensive striations located in the yellow rectangle of Fig. 11a.

rate - which is an averaged value - can differ from the local one, measured in the facets for example [50].

For each sample, an equivalent radius of the different areas described above has been measured and used to calculate an equivalent SIF range. Fig. 9a shows this equivalent SIF range corresponding to each area. [8] estimates the characteristic SIF value for crack initiation of VHCF in titanium alloys as $\Delta K = 3.39$ MPa $\sqrt{m}$. [23] evaluates the ΔK value at the Rough Area to Fish-eye transition as $\Delta K_{RA/FiE} = 9.14 \pm 1.19$ MPa $\sqrt{m}$ and claims that this value is in agreement with other studies [29,51–53]. All those literature values seem to match with the equivalent SIF range estimated in our study (Fig. 9a).

4.5. Discussion on crack growth rate

The experimental errors have been estimated from the measurement uncertainties and are presented in Appendix A. Taking these values into account, our results show that for $\Delta K < 9$ MPa $\sqrt{m}$, the crack growth rates measured for cracks propagating in vacuum ($10^{-12} < da/dN < 10^{-9}$ m/cycle) are lower than the ones measured for cracks propagating in air ($5 \times 10^{-10} < da/dN < 10^{-8}$ m/cycle). This difference can also be illustrated by the SN curves of Fig. 5b where the fatigue life of samples with a crack propagating in air is always shorter than that of a sample with a crack propagating in vacuum cycled at the same stress amplitude.[1] A close look at Fig. 9a also shows that the difference in crack growth rate between air and vacuum tends to decrease when the SIF range increases; for $\Delta K > 10$ MPa $\sqrt{m}$, some data from both environments overlap.

As described in Section 2.2, the specimen surface temperature has been monitored during cycling. For all the studied samples, no major differences could be observed in the monitored thermal emissions between samples with air-propagating cracks and samples with vacuum-propagating cracks. The temperature increase remains below 20 °C after 30 s of cycling (6×10^5 cycles at 20 kHz). Hence, it is unlikely that the differences in crack growth rate can be linked to a temperature variation.

As described in Section 4.4, the crack surface features strongly depend on the propagation environment. Once the crack has initiated but before the Fish-Eye zone ($\Delta K < 9$ MPa $\sqrt{m}$), both the crack surface features and the crack growth rates are different between air and vacuum environment suggesting very different propagation mechanisms between the two environments.

The described differences in crack surface features between the two propagation environment conditions are in agreement with the work of [49]. This reference points out – for the internal cracks which propagated in air – an "angular and sharp aspect" close to the initiation site surrounded by a "larger flat striated zone". For cracks propagating under vacuum conditions, these authors described a "granular and round aspect" in the vicinity of the initiation site which is surrounded by a "flat zone without striation".

For $\Delta K > 10$ MPa $\sqrt{m}$ – i.e. approximately at the beginning of the Fish-Eye region – the crack growth rate data for air propagation is getting closer to the vacuum data. This could mean that the propagation mechanisms for high SIF range (i.e. long cracks) are becoming similar in the two environments when cycling is performed at 20 kHz.

The relative influence of the cycling frequency and the environment has been studied for an aluminum alloy [54,55]. In this reference, the crack growth rate has been measured for cracks propagating from the sample surface under air or vacuum environment. Data have been acquired at 20 Hz and 20 kHz for loading ratios between 0.5 and −1. It was observed that (1) there is no difference in crack growth rate in vacuum between the two tested frequencies, (2) under air environment, the crack growth rate is lower if the sample is ultrasonically loaded

than if the frequency is 20 Hz. This effect increases for high SIF range values and $R = -1$, (3) the values of the decreased crack growth rates obtained with ultrasonic cycling under air environment are similar to the values obtained in vacuum conditions.

These observations are in agreement with our results on the Ti64 alloy. In [54], the influence of the cyclic frequencies is rationalized by considering the hydrogen embrittlement model from [26]: the ambient pressure is too low to allow the water vapor to be in contact with an important area of the freshly created crack surface because the crack tip is open during less than 0.025 ms (half of the loading period at 20 kHz).

This mechanism can explain why our data for internal cracks growing in vacuum presented in Fig. 9a match very well with literature data on ultra-high vacuum crack growth although the cycling frequencies are not the same. On the opposite, the air environment data seems to go from air-low-frequency-literature data towards vacuum data as the SIF range increases. It should be noted, however, that the loading ratios for several datasets presented in Fig. 9a differ from our work which limits the comparison. Additional experiments to obtain ultrasonic crack growth rate data in air environment at $R = -1$ for the studied alloy would be helpful for the comparison.

As a final remark, data obtained for sample n° 48 – orange square symbols in Fig. 9a – with air condition propagation has crack growth rates which seem to stand out and present lower da/dN than the other samples cycled under air conditions. For this sample, only relatively large values of SIF are reported because no μCT scan could be acquired when the crack was small. The 3D dataset corresponds to the crack entering the Fish-Eye zone. Despite this, the fractographic surface of this sample presents the same characteristics as the other air-propagated cracks (cf. Section 4.4) and the slope of the crack growth rate curves are the same as the other air samples so the propagation mechanisms can be assumed to be similar to the other air grown cracks.

5. Conclusions and prospects

The proposed experimental method allowed to validate the adaptation of an ultrasonic in-situ protocol (based on the setup developed by [21]) with artificial internal notches [22,23] in order to study the internal crack propagation in gigacycle fatigue regime (i.e. for low-stress amplitudes). This procedure provides access to the 3D shape of the cracks at several instants of their propagation and is adapted to the duration of a synchrotron experiment (ultrasonic loading shortens the test duration and the presence of an artificial internal notch shortens both μCT acquisition and inspection durations because the region of interest is known to be located around the notch). Based on this new type of data, the crack growth rate could be estimated for different stress intensity factor ranges during the propagation and in different environments (vacuum and air). To the best of the authors' knowledge, such experimental data could not be found in the literature for a **titanium alloy ultrasonically cycled with a stress ratio R = -1** (either under air or under vacuum environment propagation condition).

The adaptation of the protocol to air-influenced propagation brought new confirmations of the crucial impact of the environment on the crack propagation and particularly on the explanation of the very low crack growth rate of internal short crack loaded at very low-stress amplitude leading to the gigacycle regime. By connecting the artificial internal notch with the surface, we observed that internal cracks in contact with air propagate like surface cracks in air and that there is a huge difference in lifespan – for the same stress amplitudes – between cracks in contact with air and cracks under vacuum environment. These differences matched globally with literature and some observations on the crack surfaces were carried out to corroborate the environment effect. Future experiments should be carried out to confirm this conclusion on other alloys and at other loading ratios.

---

[1] [23] have shown that, with an internal laser defect, initiation represents less than 10% of the fatigue life whatever the stress level is.

CRediT authorship contribution statement

Louis Hebrard: Investigation, Methodology, Data curation, Visualization, Writing – original draft. **Jean-Yves Buffiere:** Conceptualization, Investigation, Methodology, Writing – review & editing, Supervision. **Thierry Palin-Luc:** Conceptualization, Investigation, Methodology, Writing – review & editing, Supervision. **Nicolas Ranc:** Conceptualization, Investigation, Methodology, Writing – review & editing, Supervision. **Marta Majkut:** Experimental support. **Andrew King:** Experimental support. **Arnaud Weck:** Experimental support.

Declaration of competing interest

The authors declare that they have no known competing financial interests or personal relationships that could have appeared to influence the work reported in this paper.

Data availability

Data will be made available on request.

Acknowledgments

Appendix A. Uncertainty on the quantification of the crack growth rate

The different measurements used to calculate the coordinates of the experimental data in a Paris diagram ($da/dN = f(\Delta K)$ in Fig. 9a) have uncertainties that need to be estimated.

The SIF is calculated from Eq. (3) so uncertainties need to be quantified for the stress amplitude $\sigma_a = \Delta\sigma/2$, the equivalent crack radius a_{eq} and the specimen gauge length radius b. However, as detailed in Section 4.3, the use of Eq. (3) supposes the cracks to have a penny shape which is not properly the case. Hence, the uncertainty on a_{eq} was evaluated from the radius of the smallest circle containing the projection of the crack and the radius of the largest circle contained in the projected crack. The uncertainty on the equivalent crack radius δa_{eq}, is equal to the difference between the radiuses of these two circles.

The crack growth rate is evaluated as the ratio between the crack size increase and the number of cycles between two μCT acquisitions, so uncertainties are needed for the crack size increment δa_{eq} and the increment of the number of cycles δN. The uncertainty on the extension of the projected crack area depends on the difference in the projected crack area between two successive μCT scans. The uncertainty on a_{eq} is subjectively evaluated to 5 pixels based on the capacity to distinguish the crack front in μCT data. A summary of the uncertainties estimations is presented in Table 3. Finally, the error in propagation for the SIF and the crack growth rate is computed using Eq. (4) and the results are presented in Fig. A.12:

$$\delta f(x_j) = \sqrt{\sum_j \left[\left(\frac{\partial f}{\partial x_j} \right)^2 \delta x_j^2 \right]}. \tag{4}$$

The uncertainty on the crack growth rate is negligible for high SIF but increases for smaller cracks principally because the crack growth rate is very low. The uncertainty on the SIF can be important specifically for cracks with a non-circular shape but the uncertainty level does not seem to contradict the result interpretation as the curves conserve their shape and still match literature data.

Table 3
Measurement uncertainties taken into account for the calculations.

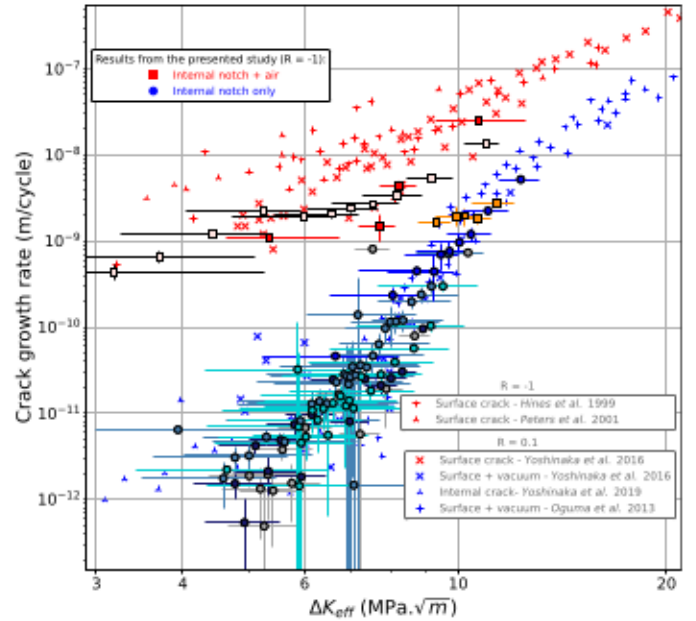| $\delta(\Delta\sigma)$	δb	δa_{eq} (for $\frac{da}{dN}$)	$\delta(\Delta N)$
2%	40 μm	5 pixels (3.5 μm)	20 cycles (1 ms)

Fig. A.12. Experimental data of this study in a Paris diagram with the illustration of uncertainties (horizontal and vertical bars) compared with literature data (for which uncertainties are unknown).

Appendix B. μCT data thresholding procedure

A μCT acquisition provides a stack of 32-bit slices which is converted to an unsigned 8-bit stack (otherwise the file size is too large for an easy treatment). The automatized thresholding protocol developed to convert each 8-bit μCT stack dataset into a binary stack representing the propagated crack is described below and illustrated in Fig. B.13:

- Fig. B.13a — Initial 8-bit grey level reconstructed slice of the crack.
- Fig. B.13b — The contrast is manually adjusted in order to increase the greyscale difference between the propagated crack and the titanium bulk. The contrast adjustment is the same for each scan of the same sample recorded after different numbers of cycles.
- Fig. B.13c — A 3D-median filter with a 3 voxels radius is applied to reduce the noise.
- Fig. B.13d — A small volume around the notch is selected in order to shorten the procedure (this volume has a cuboid shape which comprises the notch and several hundreds of voxels around it) and the threshold value is determined from the greyscale distribution of the voxels in this small volume of interest. With $D(gs)$ the number of voxels with a greyscale equal to gs in the volume, the threshold value is chosen to be the lower gs_{20} value such as $D(gs_{20}) = 0.2 \max(D)$. Hence, the overall volume is binarized to keep all the voxels with a value higher than gs_{20} (cf. Fig. B.14). The 20% value has been fixed after comparison with several sections from the original dataset (Fig. B.13a) to be sure that no important part of the crack is deleted.
- Fig. B.13e — Another 3D-median filter with a 3 voxels radius is applied to smooth the binarized volume and to remove the isolated voxels.

- Fig. B.13f — Finally, a 3D labeling tool is applied to select and delete all 3D objects smaller than a certain size. This last step allows to keep only the thresholded volume which comprises the internal notch and the propagated crack and removes spurious voxels which result from noise.
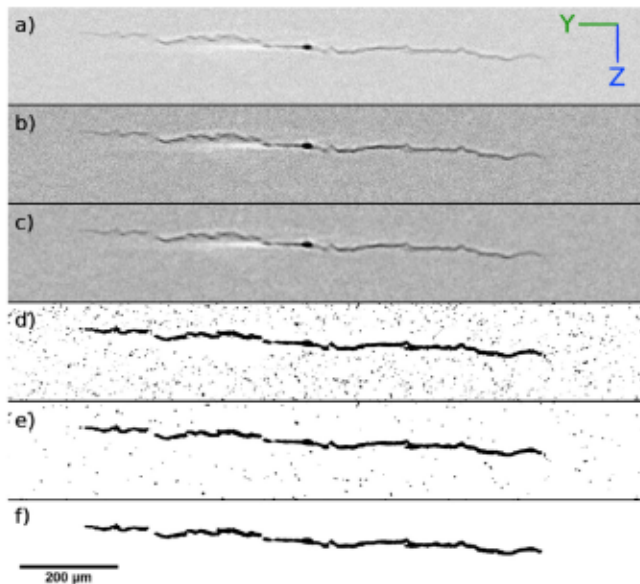

Fig. B.13. Successive steps of the thresholding protocol for a reconstructed slice of an internal crack after 4.4×10^7 cycles of propagation under vacuum with a stress amplitude of 330 MPa (specimen n° 46). The cutting plane of this section is represented in Fig. 8. (a) Initial grey level image. (f) binary image after the thresholding protocol. See the text for a detailed explanation of the successive steps (b to e). All the pictures have the same scale as (f).
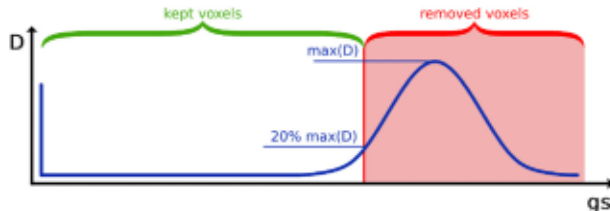

Fig. B.14. Typical grey level histogram used to determine the threshold value applied to a µCT stack.

References

[1] A. Atrens, W. Hoffelner, T.W. Duerig, J.E. Allison, Subsurface crack initiation in high cycle fatigue in Ti-6Al-4V and in a typical martensitic stainless steel, Scr. Metall. 17 (5) (1983) 601–606.

[2] Stefan Heinz, Analysis of fatigue properties and failure mechanisms of Ti6Al4V in the very high cycle fatigue regime using ultrasonic technology and 3D laser scanning vibrometry, Ultrasonics (53) (2013) 1433–1440.

[3] J. Everaerts, B. Verlinden, M. Wevers, Internal fatigue crack initiation in drawn Ti-6Al-4V wires, Mater. Sci. Technol. 32 (16) (2016) 1639–1645.

[4] J.H. Zuo, Z.G. Wang, E.H. Han, Effect of microstructure on ultra-high cycle fatigue behavior of Ti-6Al-4V, Mater. Sci. Eng. A 473 (1–2) (2008) 147–152.

[5] Y. Murakami, T. Nomoto, T. Ueda, Factors influencing the mechanism of superlong fatigue failure in steels, Fatigue Fract. Eng. Mater. Struct. 22 (1999) 581–590.

[6] Claude Bathias, P.C. Paris, Gigacycle fatigue in mechanical practice, in: M. Dekker (Ed.), Mechanical engineering, New York, NY, 2005.

[7] BEA, Accident to the AIRBUS A380-861 registered F-HPJE and operated by Air France on 30/09/2017 en route over Greenland. (Investigation delegated to BEA by the authorities of Denmark)., Rapport d'enquête, 2020, France.

[8] Youshi Hong, Chengqi Sun, The nature and the mechanism of crack initiation and early growth for very-high-cycle fatigue of metallic materials — An overview, Theor. Appl. Fract. Mech. 92 (2017) 331–350.

[9] D. Wagner, N. Ranc, C. Bathias, P.C. Paris, Fatigue crack initiation detection by an infrared thermography method, Fatigue Fract. Eng. Mater. Struct. Wiley-Blackwell 2009 (2009) 12–21.

[10] D. Krewerth, A. Weidner, H. Biermann, Application of in situ thermography for evaluating the high-cycle and very-high-cycle fatigue behaviour of cast aluminium alloy AlSi7Mg (T6), Ultrasonics 53 (8) (2013) 1441–1449.

[11] N. Ranc, A. Messager, A. Junet, T. Palin-Luc, J.Y. Buffière, N. Saintier, M. Elmay, L. Mancini, A. King, Y. Nadot, Internal fatigue crack monitoring during ultrasonic fatigue test using temperature measurements and tomography, Mech. Mater. 174 (2022) 104471.

[12] Anish Kumar, Christopher J. Torbet, J. Wayne Jones, Tresa M. Pollock, Nonlinear ultrasonics for in situ damage detection during high frequency fatigue, J. Appl. Phys. 106 (2) (2009) 024904.

[13] Y. Luo, S.C. Wu, Y.N. Hu, Y.N. Fu, Cracking evolution behaviors of lightweight materials based on in situ synchrotron X-ray tomography: A review, Front. Mech. Eng. 13 (4) (2018) 461–481.

[14] S.C. Wu, T.Q. Xiao, P.J. Withers, The imaging of failure in structural materials by synchrotron radiation X-ray microtomography, Eng. Fract. Mech. 182 (2017) 127–156.

[15] Sudhanshu S. Singh, Jason J. Williams, Peter Hruby, Xianghui Xiao, Francesco De Carlo, Nikhilesh Chawla, In situ experimental techniques to study the mechanical behavior of materials using X-ray synchrotron tomography, Integrat. Mater. Manuf. Innov. 3 (1) (2014) 109–122.

[16] T.P. Chapman, K.M. Kareh, M. Knop, T. Connolley, P.D. Lee, M.A. Azeem, D. Rugg, T.C. Lindley, D. Dye, Characterisation of short fatigue cracks in titanium alloy IMI 834 using X-ray microtomography, Acta Mater. 99 (2015) 49–62.

[17] Takashi Nakamura, Fumiyoshi Yoshinaka, Shinya Nakayama, Hiroyuki Oguma, Daiki Shiozawa, Yoshikazu Nakai, Kentaro Uesugi, Detection of small internal fatigue cracks in Ti-6Al-4V by using synchrotron radiation µCT imaging, Mech. Eng. Lett. 2 (2016) 16–00233.

[18] Gaoge Xue, Yuta Tomoda, Takashi Nakamura, Nao Fujimura, Kosuke Takahashi, Fumiyoshi Yoshinaka, Akihisa Takeuchi, Masayuki Uesugi, Kentaro Uesugi, Detection of small internal fatigue cracks in Ti-6Al-4V via synchrotron radiation nanocomputed tomography, Fatigue Fract. Eng. Mater. Struct. (2022) 1–10.

[19] Itziar Serrano-Munoz, Jean-Yves Buffière, Rajmund Mokso, Catherine Verdu, Yves Nadot, Location, location & size: defects close to surfaces dominate fatigue crack initiation, Sci. Rep. 7 (1) (2017) 45239.

[20] Diwakar Naragani, Michael D. Sangid, Paul A. Shade, Jay C. Schuren, Hemant Sharma, Jun-Sang Park, Peter Kenesei, Joel V. Bernier, Todd J. Turner, Iain Parr, Investigation of fatigue crack initiation from a non-metallic inclusion via high energy x-ray diffraction microscopy, Acta Mater. 137 (2017) 71–84.

[21] Alexandre Messager, Arnaud Junet, Thierry Palin-Luc, Jean-Yves Buffière, Nicolas Saintier, Nicolas Ranc, Mohamed El May, Yves Gaillard, Andrew King, Anne Bonnin, Yves Nadot, In situ synchrotron ultrasonic fatigue testing device for 3D characterisation of internal crack initiation and growth, Fatigue Fract. Eng. Mater. Struct. 2019 (2019).

[22] Arnaud Junet, Alexandre Messager, Xavier Boulnat, Arnaud Weck, Elodie Boller, Lukas Helfen, Jean-Yves Buffière, Fabrication of artificial defects to study internal fatigue crack propagation in metals, Scr. Mater. 171 (2019) 87–91.

[23] Arnaud Junet, Alexandre Messager, Arnaud Weck, Yves Nadot, Xavier Boulnat, Jean-Yves Buffière, Internal fatigue crack propagation in a Ti-6Al-4V alloy: An in situ study, Int. J. Fatigue 168 (2023) 107450.

[24] Y. Lenets, Crack propagation life prediction for Ti-6Al-4V based on striation spacing measurements, Int. J. Fatigue 22 (6) (2000) 521–529.

[25] M.J. Caton, R. John, W.J. Porter, M.E. Burba, Stress ratio effects on small fatigue crack growth in Ti-6Al-4V, Int. J. Fatigue 38 (2012) 36–45.

[26] R.P. Wei, G.W. Simmons, Recent progress in understanding environment assisted fatigue crack growth, Int. J. Fract. 17 (2) (1981) 235–247.

[27] R.O. Ritchie, D.L. Davidson, B.L. Boyce, J.P. Campbell, O. Roder, High-cycle fatigue of Ti-6Al-4V, Fatigue Fract. Eng. Mater. Struct. 22 (7) (1999) 621–631.

[28] H. Oguma, T. Nakamura, Fatigue crack propagation properties of Ti-6Al-4V in vacuum environments, Int. J. Fatigue 50 (2013) 89–93.

[29] Fumiyoshi Yoshinaka, Takashi Nakamura, Kazuaki Takaku, Effects of vacuum environment on small fatigue crack propagation in Ti-6Al-4V, Int. J. Fatigue 91 (2016) 29–38.

[30] J. Petit, C. Sarrazin-Baudoux, J. Martinez, S. Stanzl-Tschegg, H. Mayer, Very high cycle fatigue behavior of a Ti6246 alloy in air and in high vacuum, in: Fourth International Conference on Very High Cycle Fatigue (VHCF-4), 2007.

[31] V. Sinha, J.M. Larsen, Vacuum levels needed to simulate internal fatigue crack growth in titanium alloys and nickel-base superalloys: thermodynamic considerations, Metall. Mater. Trans. A 43 (10) (2012) 3433–3441.

[32] J. Petit, C. Sarrazin-Baudoux, An overview on the influence of the atmosphere environment on ultra-high-cycle fatigue and ultra-slow fatigue crack propagation, Int. J. Fatigue 28 (11) (2006) 1471–1478.

[33] Gilbert Hénaff, Christine Sarrazin-Baudoux, Environmentally Assisted Fatigue in the Gaseous Atmosphere, in: Comprehensive Structural Integrity, Elsevier, 2023, pp. 45–130.

[34] H. Oguma, T. Nakamura, The effect of stress ratios on very high cycle fatigue properties of Ti-6Al-4V, Key Eng. Mater. 261–263 (2004) 1227–1232.

[35] Jaap Schijve, Internal fatigue cracks are growing in vacuum, Eng. Fract. Mech. 10 (1978) 359–370.

[36] B.A. Cowles, High cycle fatigue in aircraft gas turbines—an industry perspective, Int. J. Fract. 80 (2–3) (1996) 147–163.

[37] M. Janeček, F. Nový, P. Harcuba, J. Stráský, L. Trško, M. Mhaede, L. Wagner, The very high cycle fatigue behaviour of Ti-6Al-4V alloy, Acta Phys. Polon. A 128 (4) (2015) 497–503.

[38] Zhi Yong Huang, Qing Yuan Wang, Danièle Wagner, Claude Bathias, A very high cycle fatigue thermal dissipation investigation for titanium alloy TC4, Mater. Sci. Eng. A 600 (2014) 153–158.

[39] F. Berto, A. Campagnolo, P. Lazzarin, Fatigue strength of severely notched specimens made of Ti-6Al-4V under multiaxial loading, Fatigue Fract. Eng. Mater. Struct. 38 (5) (2015) 503–517.

[40] Xiaolong Liu, Chengqi Sun, Youshi Hong, Effects of stress ratio on high-cycle and very-high-cycle fatigue behavior of a Ti–6Al–4V alloy, Mater. Sci. Eng. A 622 (2015) 228–235.

[41] E. Takeuchi, Y. Furuya, N. Nagashima, S. Matsuoka, The effect of frequency on the giga-cycle fatigue properties of a Ti-6al-4v alloy, Fatigue Fract. Eng. Mater. Struct. 31 (7) (2008) 599–605.

[42] Hiroshi Tada, Paul C. Paris, George R. Irwin, The Stress Analysis of Cracks Handbook, Third Edition, American Society of Mechanical Engineers Press, 2000.

[43] J.A. Hines, G. Lutjering, Propagation of microcracks at stress amplitudes below the conventional fatigue limit in Ti-6Al-4V, Fatigue Fract. Eng. Mater. Struct. 22 (8) (1999) 657–665.

[44] J.O. Peters, G. Lutjering, Comparison of the fatigue and fracture of $\alpha + \beta$ and β titanium alloys, Metall. Mater. Trans. A (2001) 14.

[45] Fumiyoshi Yoshinaka, Takashi Nakamura, Akihisa Takeuchi, Masayuki Uesugi, Kentaro Uesugi, Initiation and growth behaviour of small internal fatigue cracks in Ti-6Al-4V via synchrotron radiation microcomputed tomography, Fatigue Fract. Eng. Mater. Struct. 2019 42 (2019) 2093–2105.

[46] A.J. McEvily, T. Nakamura, H. Oguma, K. Yamashita, H. Matsunaga, M. Endo, On the mechanism of very high cycle fatigue in Ti–6Al–4V, Scr. Mater. 59 (11) (2008) 1207–1209.

[47] J.C. Newman, A nonlinear fracture mechanics approach to the growth of small cracks. in behavior of short cracks in airframe components, in: Neuilly sur Seine (France): Advisory Group for Aerospace Research and Development. Proceedings, Vol. 328, 1983, pp. 6.1–20.

[48] R.M.N. Pelloux, Mechanisms of formation of ductile fatigue striations, Trans. Am. Soc. Metals 62 (1969) 281–285.

[49] Fumiyoshi Yoshinaka, Gaoge Xue, Nao Fujimura, Takashi Nakamura, Effect of vacuum pressure on small crack propagation in Ti-6Al-4V, Int. J. Fatigue 142 (2021) 105961.

[50] Jason J. Williams, Kyle E. Yazzie, N. Connor Phillips, Nikhilesh Chawla, Xinghui Xiao, Francesco De Carlo, Nagaraja Iyyer, Maddan Kittur, On the correlation between fatigue striation spacing and crack growth rate: A three-dimensional (3-d) X-ray synchrotron tomography study, Metall. Mater. Trans. A 42 (13) (2011) 3845–3848.

[51] Fei Cao, K.S. Ravi Chandran, The role of crack origin size and early stage crack growth on high cycle fatigue of powder metallurgy Ti-6Al-4V alloy, Int. J. Fatigue 102 (2017) 48–58.

[52] Wei Li, Hongqiao Zhao, Abdelhak Nehila, Zhenyu Zhang, Tatsuo Sakai, Very high cycle fatigue of TC4 titanium alloy under variable stress ratio: Failure mechanism and life prediction, Int. J. Fatigue 104 (2017) 342–354.

[53] S. Heinz, D. Eifler, Crack initiation mechanisms of Ti6Al4V in the very high cycle fatigue regime, Int. J. Fatigue 93 (2016) 301–308.

[54] B. Holper, Near threshold fatigue crack growth in aluminium alloys at low and ultrasonic frequency: Influences of specimen thickness, strain rate, slip behaviour and air humidity, Int. J. Fatigue 25 (5) (2003) 397–411.

[55] Stefanie Stanzl-Tschegg, Very high cycle fatigue measuring techniques, Int. J. Fatigue 60 (2013) 2–17.